Mapping astrocyte activity domains by light sheet imaging and spatio-temporal correlation screening

Cuong Pham, Daniela Herrera Moro, Christine Mouffle, Steve Didienne, Régine Hepp, Frank Pfrieger, Jean-Marie Mangin, Pascal Legendre, Claire Martin, Serge Luquet, et al.

NeuroImage 220 (2020) 117069

Contents lists available at ScienceDirect

NeuroImage

journal homepage: www.elsevier.com/locate/neuroimage

Mapping astrocyte activity domains by light sheet imaging and spatio-temporal correlation screening

Cuong Pham [a], Daniela Herrera Moro [b], Christine Mouffle [a], Steve Didienne [a], Régine Hepp [a], Frank W. Pfrieger [c], Jean-Marie Mangin [a], Pascal Legendre [a], Claire Martin [b], Serge Luquet [b], Bruno Cauli [a], Dongdong Li [a,*]

[a] Sorbonne Université, Institute of Biology Paris Seine, Neuroscience Paris Seine, CNRS UMR8246, INSERM U1130, UPMC UMCR18, Paris, 75005, France
[b] Unité de Biologie Fonctionnelle et Adaptative, Centre National la Recherche Scientifique, Unité Mixte de Recherche 8251, Université Paris Diderot, Sorbonne Paris Cité, 75205, Paris, France
[c] Centre National de la Recherche Scientifique, Université de Strasbourg, Institut des Neurosciences Cellulaires et Intégratives, F-67000, Strasbourg, France

ARTICLE INFO

Keywords:
Fluorescence
Calcium
GCaMP
Brain

ABSTRACT

Astrocytes are a major type of glial cell in the mammalian brain, essentially regulating neuronal development and function. Quantitative imaging represents an important approach to study astrocytic signaling in neural circuits. Focusing on astrocytic Ca^{2+} activity, a key pathway implicated in astrocye-neuron interaction, we here report a strategy combining fast light sheet fluorescence microscopy (LSFM) and correlative screening-based time series analysis, to map activity domains in astrocytes in living mammalian nerve tissue. Light sheet of micron-scale thickness enables wide-field optical sectioning to image astrocytes in acute mouse brain slices. Using both chemical and genetically encoded Ca^{2+} indicators, we demonstrate the complementary advantages of LSFM in mapping Ca^{2+} domains in astrocyte populations as compared to epifluorescence and two-photon microscopy. Our approach then revealed distinct kinetics of Ca^{2+} signals between cortical and hypothalamic astrocytes in resting conditions and following the activation of adrenergic G protein coupled receptor (GPCR). This observation highlights the activity heterogeneity across regionally distinct astrocyte populations, and indicates the potential of our method for investigating dynamic signals in astrocytes.

1. Introduction

As a major type of glial cell, astrocytes form interconnected networks in mammalian central nervous system (Giaume et al., 2010). Long thought as solely supportive elements in nervous tissue, astrocytes are now being revealed as critical players in brain development and function (Dallerac et al., 2018). Astrocyte activity is encoded by dynamic intra- and intercellular signals that regulate synaptic microenvironment, communications within neural circuits and cognition (Santello et al., 2019). Spatio-temporal characterization of astrocytic signals in situ is the premise to understand their contribution to central information processing. With the continuous development of fluorescent indicators for specific signaling pathways (Deo and Lavis, 2018; Lin and Schnitzer, 2016; Lobas et al., 2019), dynamic imaging stands as an important approach to investigate astrocyte function.

As a highly dynamic signal, intracellular Ca^{2+} oscillation represents an important aspect of astrocyte activity that occurs spontaneously or downstream of GPCR activation by neurotransmitters (Agulhon et al., 2008; Khakh and McCarthy, 2015). Such Ca^{2+} signaling has been implicated in gliotransmitter release, neurotransmitter and ion homeostasis, neurovascular coupling and perisynaptic structural remodeling (Bazargani and Attwell, 2015; Cauli and Hamel, 2018; Khakh and McCarthy, 2015; Nedergaard and Verkhratsky, 2012). Recent evidence suggests the involvement of astrocyte Ca^{2+} signal in the central control of animal behaviors (Covelo and Araque, 2018; Robin et al., 2018). Furthermore, departing from the conventional view that astrocytes form a homogeneous cohort, recent studies also start to notice their heterogeneities in terms of gene expression, morphology and functional interaction with local neural circuits (Chai et al., 2017; Lanjakornsiripan et al., 2018; Martin-Fernandez et al., 2017). Nevertheless, both the cellular mechanism and the functional consequence of astrocytic Ca^{2+} signal still remain debated (Bazargani and Attwell, 2015; Fiacco and McCarthy,

* Corresponding author.
E-mail address: dongdong.li@inserm.fr (D. Li).

https://doi.org/10.1016/j.neuroimage.2020.117069
Received 3 April 2020; Received in revised form 12 June 2020; Accepted 15 June 2020
Available online 22 June 2020

2018; Savtchouk and Volterra, 2018). A better understanding of the spatial and temporal features of astrocytic Ca^{2+} signals in situ will help to dissect their functions in the nervous system.

Optical microscopes combined with high-affinity Ca^{2+} sensors have enabled dynamic imaging of astrocytic Ca^{2+} in various contexts (Otsu et al., 2015; Perez-Alvarez et al., 2014; Reeves et al., 2011). Epifluorescence (EPI) microscopy coupled with digital cameras allows fast wide-field imaging, whereas the image contrast is degraded by out-of-focus fluorescence due to the lack of optical sectioning. This problem could be ameliorated by computational deconvolution using theoretical or empiric point spread function (Li et al., 2004; Swedlow, 2013), yet this method usually requires off-line and time-consuming iterative computations. Direct optical sectioning has been achieved by laser scanning confocal and two-photon microscopy, which evidently improves the image quality (Otsu et al., 2015; Shigetomi et al., 2013), yet also imposes limitations on imaging speed due to the spatial scanning (Keller and Ahrens, 2015; Svoboda and Yasuda, 2006). Also, during laser scanning, the high local energy of the focused beam may disturb astrocyte Ca^{2+} homeostasis (Kuga et al., 2011; Schmidt and Oheim, 2018; Zhao et al., 2009). Moreover, the relatively high cost of the femtosecond pulsed lasers required for two-photon microscopy limits its wide application. It is therefore desirable to achieve optical sectioning in a scanless manner for in situ astrocyte Ca^{2+} imaging.

Light sheet of micron-scale thickness can be generated from continuous wave lasers by objectives of long focal depth (Keller and Dodt, 2012; Ritter et al., 2010). Aligning light sheet orthogonally to the focal plane of an imaging objective enables scanless wide-field optical sectioning and ultrafast image acquisition by digital cameras (Ahrens et al., 2013; Jemielita et al., 2013; Power and Huisken, 2017). Here, we adopted light sheet imaging to characterize astrocyte Ca^{2+} dynamics in acute mouse brain slices. In parallel, a computational principle based on spatio-temporal correlation screening was introduced to map active Ca^{2+} domains. Using chemical and genetically encoded indicators, we demonstrated the ability of light sheet imaging to resolve astrocyte Ca^{2+} activity. Video rate acquisition was achieved over wide field up to hundreds of microns with adapted objectives. Using this method, we observed distinct Ca^{2+} kinetics between cortical and hypothalamic astrocytes in resting condition and in response to GPCR activation, lending support to the activity heterogeneities associated with local astrocyte populations. Light sheet imaging therefore represents a useful tool to study astrocyte activity and its diversity in mammalian nerve tissues, and will complement the methods to investigate glial functions.

2. Materials and methods

2.1. Preparation of mouse brain slices

Experiments were undertaken in accordance with European Community guiding principles on the care and use of animals (86/609/CEE), and the rules of the host institute. Coronal slices comprising

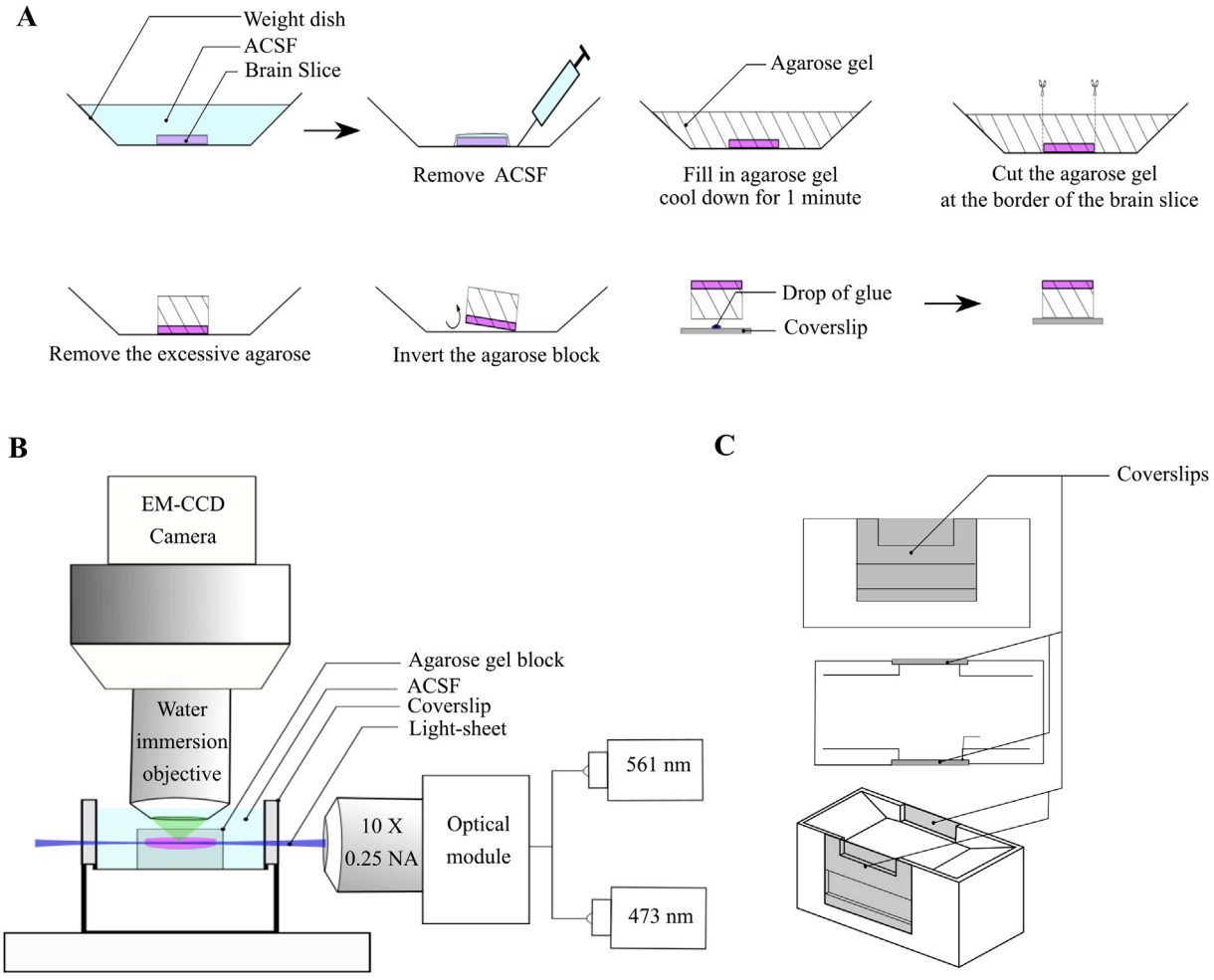

Fig. 1. Procedures and setup for light-sheet imaging. **(A)** Illustration of the placement of brain slices. **(B)** A light sheet optical module was orthogonally conjugated to an existing upright microscope. Two laser lines were coupled to the optical module via a fiber combiner. An air objective of long-working distance (× 10, 0.25 NA) was used to generate a thin and elongated light sheet for in-focus excitation. **(C)** The holding chamber designed for lateral light sheet excitation. From left to right: side, top and iso view.

somatosensory cortex and hypothalamus were acutely prepared from C57BL/6 mice of both sexes at ages as indicated. Mice were deeply anesthetized by isoflurane (Axcience) evaporation in a closed plexiglass box. For mice less than 4 weeks old, the brain was taken out and placed in ice-cold artificial cerebrospinal fluid (aCSF, mM: 124 NaCl, 4.5 KCl, 1.2 NaH_2PO_4, 1 $MgCl_2$, 2 $CaCl_2$, 26 $NaHCO_3$, and 10 D-Glucose), and cut into 300-μm thick slices by a vibratome (Leica VT1200S). For mice older than 4 weeks, the brain was placed in a modified aCSF for slicing (in mM: 30 NaCl, 4.5 KCl, 1.2 NaH_2PO_4, 1 $MgCl_2$, 26 $NaHCO_3$, 10 D-Glucose, and 194 sucrose) (Jiang et al., 2016) maintained at 4 °C during sectioning. Brain slices were recovered in normal aCSF at 37 °C for about 1 h. Prior to imaging, one single slice was mounted on a block of liquid-state transparent agarose (2% low melting agarose, Thermo Scientific). When cooled, the sample-containing agarose block was glued on 10-mm glass coverslip and then together placed in the light sheet imaging chamber (Fig. 1A). Fluorescent beads (#1851011, Thermo Fisher Scientific) were diluted 10-fold in distilled water and dispersed directly into a drop of agarose. Imaging was carried out at room temperature (21–23 °C) under constant perfusion (~3 ml/min) with aCSF. Solutions were saturated with a mixture of 95% O_2 and 5% CO_2.

2.2. Ex vivo and in vivo labeling of astrocytes

For ex vivo labeling, astrocytes were vitally stained by the red fluorescent dye sulforhodamine 101 (SR101) (Sigma-Aldrich) (Appaix et al., 2012; Nimmerjahn et al., 2004). Brain slices were incubated in aCSF containing 5 μM SR101 for 1 h in the dark and continuously bubbled with a mixture of 95% O_2 and 5% CO_2. After labeling, the slices were thoroughly washed in dye-free aCSF for at least 15 min prior to imaging. A similar procedure was used to load the Ca^{2+}-sensitive dye Fluo2 AM (TEF Labs; 5 μM, 1 h) in astrocytes in slices of ~3–4 weeks old mice. Mice of similar age were used also for in vivo labeling of astrocytes, sulforhodamine B (10 mg/ml, Sigma) was intraperitoneally injected into awake mice at a dose of 10 μL/g (Appaix et al., 2012; Perez-Alvarez et al., 2013). The genetically encoded Ca^{2+} indicator GCaMP6 was expressed in astrocytes in vivo by crossing a Cre-dependent GCaMP6f mouse line (Ai95, The Jackson Laboratory) with an astrocyte-specific Glast-CreER^{T2} mouse line (Slezak et al., 2007). Tamoxifen (T5648, Sigma-Aldrich) or its active metabolite 4-Hydroxytamoxifen (4-OHT) (Sigma-Aldrich or Tocris) were first dissolved in ethanol and aliquoted at 1 mg/50 μL. Corn oil (Sigma-Aldrich) was then added to each aliquot to reconstitute at 1 mg/250 μL, which was then warmed at 37 °C for 15 min and sonicated for 15 min until the solution was clear. Aliquots were stored at −20 °C until use. For 4-OHT, one dose of 1 mg was intraperitoneally injected in GCaMP6f/-Glast-CreER^{T2} bigenic mice at ~3–4 weeks of age. When using tamoxifen, mice were injected once a day (1 mg) for two consecutive days. Imaging experiments were carried out about two weeks after the last injection.

2.3. Imaging setups and procedures

Light sheet imaging was performed using a custom-built setup based on a wide-field upright microscope (Zeiss Axioskop 50, Germany) equipped with water-immersion objectives (Fig. 1B). EPI illumination was provided by a monochromator light source (Polychrome II, TILL Photonics, Germany) directly coupled to the imaging objective via an optical fiber. We used three water immersion imaging objectives: × 10 NA0.3, × 20 NA0.5 and × 40 NA0.8 (ZEISS). The green fluorescence of Fluo2 and GCaMP6 was separated from the red fluorescence of SR101, by spectrally exclusive double-band filters (Di03-R488/561-t3 and FF01-523/610, Semrock). Fluorescence signal was collected using a digital electron-multiplying charge-coupled device (EMCCD Cascade 512B, Photometrics).

The in-focus light sheet was generated from an independent optical module (Alpha3 light sheet add-on, Phaseview, France) equipped with an air objective (Zeiss EC EPIPlan × 10, 0.25NA). This optical module was orthogonal to the upright imaging pathway and coupled via a wavelength combiner (Thorlabs) to two continuous wave lasers (473-nm and 561-nm, CNI) (Fig. 1A). The center thickness (ω) of the generated light sheet was in the order of ~1–2 μm (Power and Huisken, 2017):

$$\omega = \frac{2\lambda}{\pi NA} \quad (1)$$

where λ denotes laser wavelength, NA the numerical aperture of excitation objective and π the Archimede's constant. The center of light sheet was orthogonally aligned to the focus of the imaging objective, so as to achieve wide-field optical sectioning (Fig. 1B). A chamber for light sheet imaging (20 × 30 × 46 mm width, height and length) was custom-designed using 3D modeling software (Trimble SketchUP; Fig. 1C), and produced by a Mojo 3D printer (Stratasys). Two 22 × 22 mm glass coverslips (#1, Erie Science Company, USA) were glued (Dow Corning GmbH, Germany) to each side of the chamber, thereby enabling the lateral illumination. The chamber was mounted on a motorized PI stage (Physik Instrumente GmbH, Germany) for axial micro-manipulation. Laser excitation and image acquisition were controlled by MetaMorph (Molecular Devices).

Two-photon imaging was performed using a custom-built setup as reported previously (Bonnot et al., 2014). It was based on an upright microscope (BX51WI, Olympus) equipped with a × 40 NA0.8 water immersion objective (Olympus) and a tunable femtosecond Ti:sapphire pulsed laser (MaiTai HP; Spectra Physics, Ellicot City, MD, USA). For SR101 and GCaMP6 imaging, two-photon excitation was set at 850 nm and at 880 nm, respectively (Appaix et al., 2012; Mutze et al., 2012). Fluorescence emitted by SR101 and GCaMP6 was split by a dichroic mirror at 590 nm, filtered subsequently by either a 535/50 nm or a 615/45 nm bandpass filter, respectively and collected by two independent photomultipliers (PMT H9305-03, Hamamatsu). Image acquisition was performed using the Matlab routine ScanImage (Pologruto et al., 2003). When × 40 NA0.8 water immersion objective was used, the lateral pixel size of two-photon imaging was set to 0.34 μm, comparable to EPI/LSFM CCD imaging (0.4 μm). To obtain fluorescence profiles along the *z*-axis, the sample was moved vertically in a step size of 0.5 μm.

2.4. Fluorescent immunohistochemistry and genotyping

Bigenic mice expressing GCaMP6 in astrocytes were anesthetized by intraperitoneal injection of pentobarbital at lethal dose (200 μl, Euthasol Vet, Dechra), and then subjected to intracardiac perfusion of phosphate buffer solution (PBS) for blood removal followed by infusion of 4% paraformaldehyde (PFA, Sigma-Aldrich). Harvested brains were fixed in 4% PFA overnight, prior to being washed in PBS containing 30% sucrose and 0.09% NaN_3. Tissues were next embedded in optimal cutting temperature compound (VWR, Fontenay-sous-bois, France) and quickly frozen at −50 °C in isopentane. Thirty μm thick floating coronal slices were cut using a cryostat (Leica, Wetzlar, Germany), washed in PBS and then incubated for 1 h in a blocking solution (0.25% fish gelatin with 0.4% Triton X-100 in PBS). Primary antibodies were diluted in the same solution, and added to slices overnight at 4 °C (rabbit monoclonal anti-S100β, ab52642, Abcam, Cambridge, UK, diluted at 1/500; chicken polyclonal anti-GFP, Aves Labs, Davis, CA, USA, diluted at 1/1000). After being washed in PBS, brain slices were incubated at room temperature for 2 h with the secondary antibodies diluted in the blocking solution (Alexa fluor 488- and 594-conjugated antibodies, Thermofisher, Waltham, MA, USA), to detect rabbit monoclonal and chicken polyclonal primary antibodies, respectively. After thorough washing, brain slices were dried and mounted in Mowiol medium (Millipore, Darmstadt, Germany). Fluorescent images of dual-color immunostaining were obtained using a standard confocal microscope (Zeiss LSM 800, Germany).

Genotyping of the Cre-dependent GCaMP6f mouse line (Ai95, The Jackson Lab) used the standard primers and polymerase chain reaction protocols provided by the supplier. Genotyping of GLAST-CreER^{T2} mouse line was performed using the primers for Cre recombinase (TK139/141)

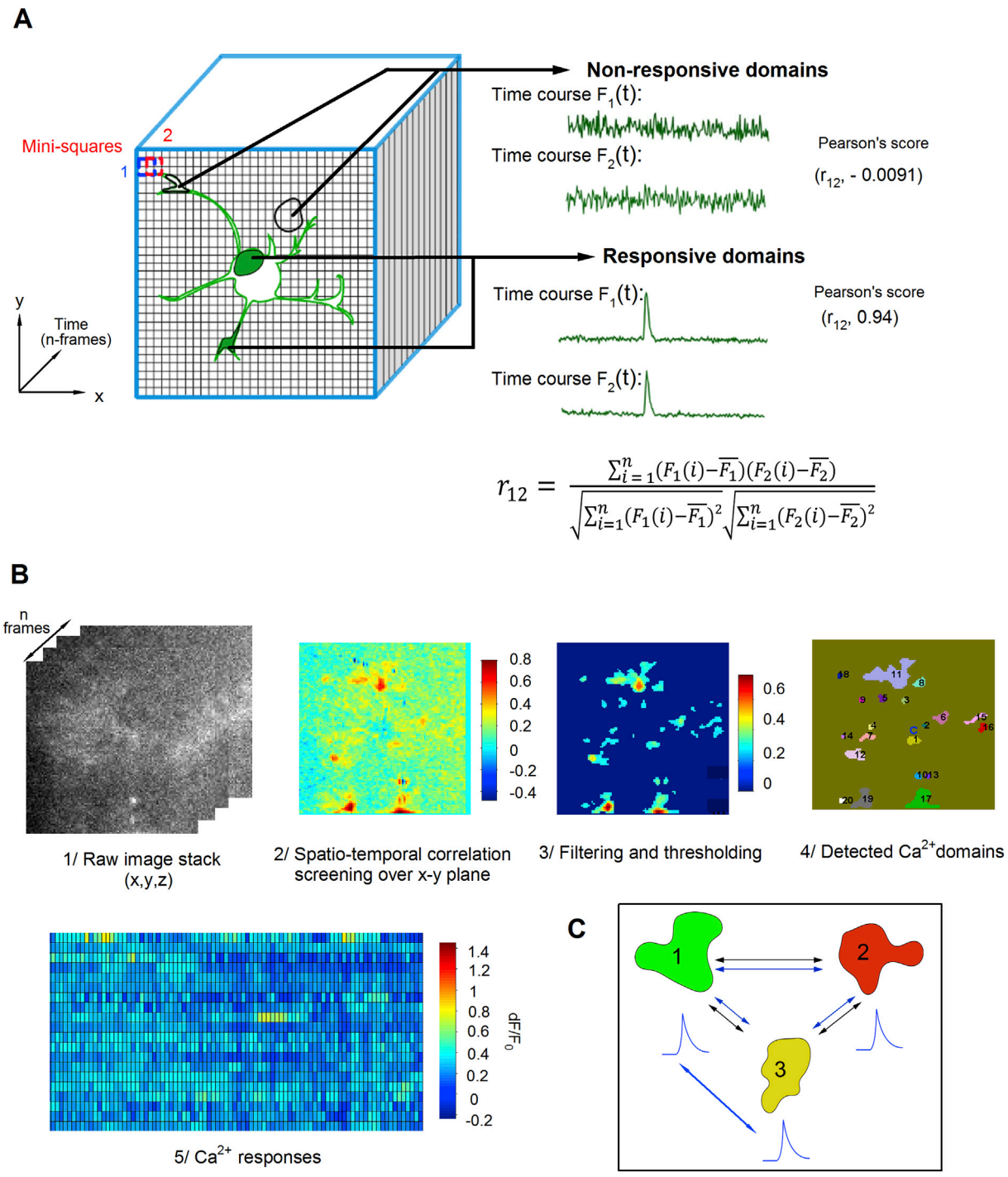

$$r_{12} = \frac{\sum_{i=1}^{n}(F_1(i)-\overline{F_1})(F_2(i)-\overline{F_2})}{\sqrt{\sum_{i=1}^{n}(F_1(i)-\overline{F_1})^2}\sqrt{\sum_{i=1}^{n}(F_2(i)-\overline{F_2})^2}}$$

Fig. 2. Mapping astrocytic Ca^{2+} domains by screening locally correlated temporal signals. (A) Spatio-temporal correlation screening. Time-lapse image stack was obtained by acquiring consecutively the focal plane image of living nerve tissue. Time courses of contiguous pixels in Ca^{2+}-active domains (shaded in green) show higher correlation level than those of inactive domains and background regions. **(B)** Principal steps for C-Screen mapping. **(C)** Spatial and temporal parameters can be extracted following the identification of Ca^{2+}-active domains. For instance, the temporal correlation (r_{ij}) can be derived for Ca^{2+} signals between all paired combinations of active domains. Its distribution offers a global estimation on the synchronization degree of Ca^{2+} signals. In parallel, corresponding domain-domain distances (d_{ij}) can also be derived from their centroid coordinates.

as reported (Slezak et al., 2007).

2.5. Detection of Ca^{2+} domains by spatio-temporal correlation screening

Astrocyte Ca^{2+} signals acquired with current technology appear as local bursts or as wide-spread increases of fluorescence intensity over multiple pixels as previously observed (Otsu et al., 2015; Reeves et al., 2011; Shigetomi et al., 2010). Given that the time-dependent intensity changes of contiguous pixels within a defined Ca^{2+} domain are highly synchronized, we devised a computational method to screen for

temporally correlated Ca^{2+} signals so as to detect discrete Ca^{2+} domains. The Pearson's correlation coefficient r_{12} between time courses of half-overlapping mini-squares (2×2 pixel^2) was calculated in a running manner across the *x-y* image plane (Fig. 2A):

$$r_{12} = \frac{\sum_{i=1}^{n}(F_1(i) - \overline{F_1})(F_2(i) - \overline{F_2})}{\sqrt{\sum_{i=1}^{n}(F_1(i) - \overline{F_1})^2}\sqrt{\sum_{i=1}^{n}(F_2(i) - \overline{F_2})^2}} \quad (2)$$

where F_1 and F_2 representing the time courses derived from the two mini-squares and n representing the total number of image frames contained in a single movie. The time axis designates the third dimension in the movie (i.e., the time-lapse image stack). As expected, the r_{12} value between running mini-squares appeared higher in Ca^{2+}-active domains than areas showing no evident Ca^{2+} rises as dominated by background noises (exemplified in Fig. 2A). This approach enabled the detection of Ca^{2+} domains in time series images. Prior to analysis, we subtracted from the raw images the background signal as determined by the minimal intensity projection of the entire stack.

Computing temporal r_{12} correlation values of the overlapping mini-squares in a running manner across the *x-y* image plane (*z* as the time axis) gave rise to a 2D correlation map (Fig. 2B). This map was then segmented by an empirically determined correlation threshold (0.14–0.2) based on the match to the visual inspection of original movies. Subsequently, a low-pass median filter (3 - 5 pixel size) was applied to remove scattered solitary pixels. A signal threshold was further applied to determine Ca^{2+} domains, with their mean fluorescence time course comprising at least three consecutive data points exceeding three times standard deviation of the baseline. The baseline was searched by running a temporal segment (20 data points in length) across the full time course of single domains to find a period showing minimum mean intensity. The Ca^{2+} signal of single domains was then normalized as dF/F_0, with F_0 representing the mean baseline intensity (Fig. 2B). To quantify the signal strength, we calculated the temporal integral for normalized Ca^{2+} responses over a unitary time period (/minute). The detection of Ca^{2+}-active domains enables the further extraction of spatio-temporal information on astrocyte activity. This included the temporal correlations between Ca^{2+} signals across all combined detected domains (Fig. 2C), which indicates the degree of global signal synchronization. In addition, domain-domain distances could also be derived by their centroid coordinates (Fig. 2C). Since this method is based on correlation screening, we abbreviate it as C-Screen.

2.6. Fluorescent object analysis

The apparent size of fluorescent objects was derived from their center linescan profile obtained with ImageJ (NIH). The linescan profile was fitted with a Gaussian curve in Igor Pro (WaveMetrics), and the full width at half maximum (FWHM) served as size estimate. The minimal intensity of the image or the minimum projection of a temporal stack was used as background signal and subtracted from the raw images. Signal-to-background ratios (SBRs) of fluorescent objects were also derived from their linescan profile, calculated as the ratio of the peak against the basal level intensity.

2.7. Statistics

Experimental data are expressed as mean ± standard error unless otherwise mentioned. The *t*-test was performed for two-group comparisons, and significant difference was determined by *p* values less than 0.05. Mann-Whitney *U* test was also used to ascertain the significance level, in considering the deviation of the experimental data from the theoretical symmetrical distribution. In the present study, these two test methods yielded consistent results on statistic significance. Statistical tests were carried out in Matlab (The MathWorks). The significance levels are shown in figures by *$p < 0.05$, **$p < 0.01$, ***$p < 0.001$.

3. Results

3.1. Spatial performance of LSFM imaging

Prior to imaging astrocytes in brain tissue, we validated the performance of LSFM using micron-scale green fluorescent beads (core size, ~0.5 μm). Dispersed fluorescent puncta were observed in both LSFM and EPI images. Whereas EPI images appeared blurred due to out-of-focus fluorescence (Fig. 3A), LSFM images revealed single fluorescence beads at much higher contrast due to the optical sectioning (Fig. 3A). Linescan profiles confirmed the sharper fluorescence distribution obtained with LSFM (Fig. 3B). We next examined the fluorescence distribution of single beads along *z*-axis. An appreciable elongation along the *z*-axis was observed in EPI images, reflecting the low effective resolution along this axis (Li et al., 2004). This distortion was reduced by light sheet sectioning that revealed significantly shorter *z* profiles for single beads (Fig. 3C–D). To gain a comparative clue between our one-photon light sheet system and two-photon microscopy, we used both approaches to image the fluorescent beads. While two-photon microscope yielded the most contrasted image, the improvement provided by LSFM lied in the comparable range particularly along the *z*-axis (Fig. S1A-B). The out-of-focus fluorescence was further investigated using fluorescent beads (core size, ~4 μm) of similar size as astrocytic somata and their main branches (Shigetomi et al., 2013). In the *y-z* projection plane, the lateral (i.e., along *y*-axis) intensity was analyzed at both the focal and out-of-focus positions. Out-of-focus fluorescence at 10 μm above and below the focal plane was high in EPI images, but greatly reduced by LSFM (Fig. 3E). Hence, wide-field optical sectioning using LSFM ensures high spatial imaging performance.

3.2. Imaging astrocytes in acute brain tissues

Essential in regulating neural circuit function, astrocytes are widely distributed across brain regions (Giaume et al., 2010; Santello et al., 2019). They bear satellite branches and processes sitting in close contact to neuronal synapses and blood vessels, setting an architectural composition for neuroglial communication (Cauli and Hamel, 2018; Giaume et al., 2010). We then used LSFM to visualize astrocytes in acute mouse cortical slices after ex vivo labeling with astrocyte-specific fluorescent dye SR101 (Appaix et al., 2012; Nimmerjahn et al., 2004). Selective labeling was confirmed by colocalization with EGFP-positive astrocytes in the ALDH1L1-EGFP transgenic mouse line (Cahoy et al., 2008) (Fig. S2A). SR101-labeled astrocytes were well resolved by LSFM, whereas corresponding EPI images were blurred by out-of-focus signals (Fig. 4A and B). The signal-to-background ratio (SBR) was about three times higher with LSFM compared to EPI (Fig. 4C; $p < 0.01$). LSFM revealed SR101-labeled astrocytic branches (Fig. 4D), as observed also by two-photon microscopy in brain slices (Fig. S1C) and in vivo (Nimmerjahn et al., 2004), which however were barely visible in EPI images (Fig. 4D). The superior performance of LSFM was also evident when using a low-magnification objective to extend the field of view (Fig. 4E and F). To corroborate these observation, we also performed in vivo labeling of astrocytes through injection of the red fluorescent dye sulforhodamine B in awake mice, as reported previously (Appaix et al., 2012; Perez-Alvarez et al., 2013). The labeled astrocytes and their branches were also resolved by LSFM in the acute brain slice (Fig. S2B).

3.3. Light sheet imaging of astrocytic Ca^{2+} signal

We then used LSFM to image Ca^{2+} signals in astrocytes in acute mouse cortical slices. Chemical fluorescent Ca^{2+} indicators are convenient to use and allow sensitive optical detection of subcellular Ca^{2+} events (Lock et al., 2015). We used a green-fluorescent chemical indicator Fluo2 AM, a member of the membrane-permeable acetoxymethyl ester (AM) Ca^{2+} dyes that label astrocytes in slice preparations (Fiacco et al., 2007; Reeves et al., 2011). Indeed, Fluo2 labeling colocalized with

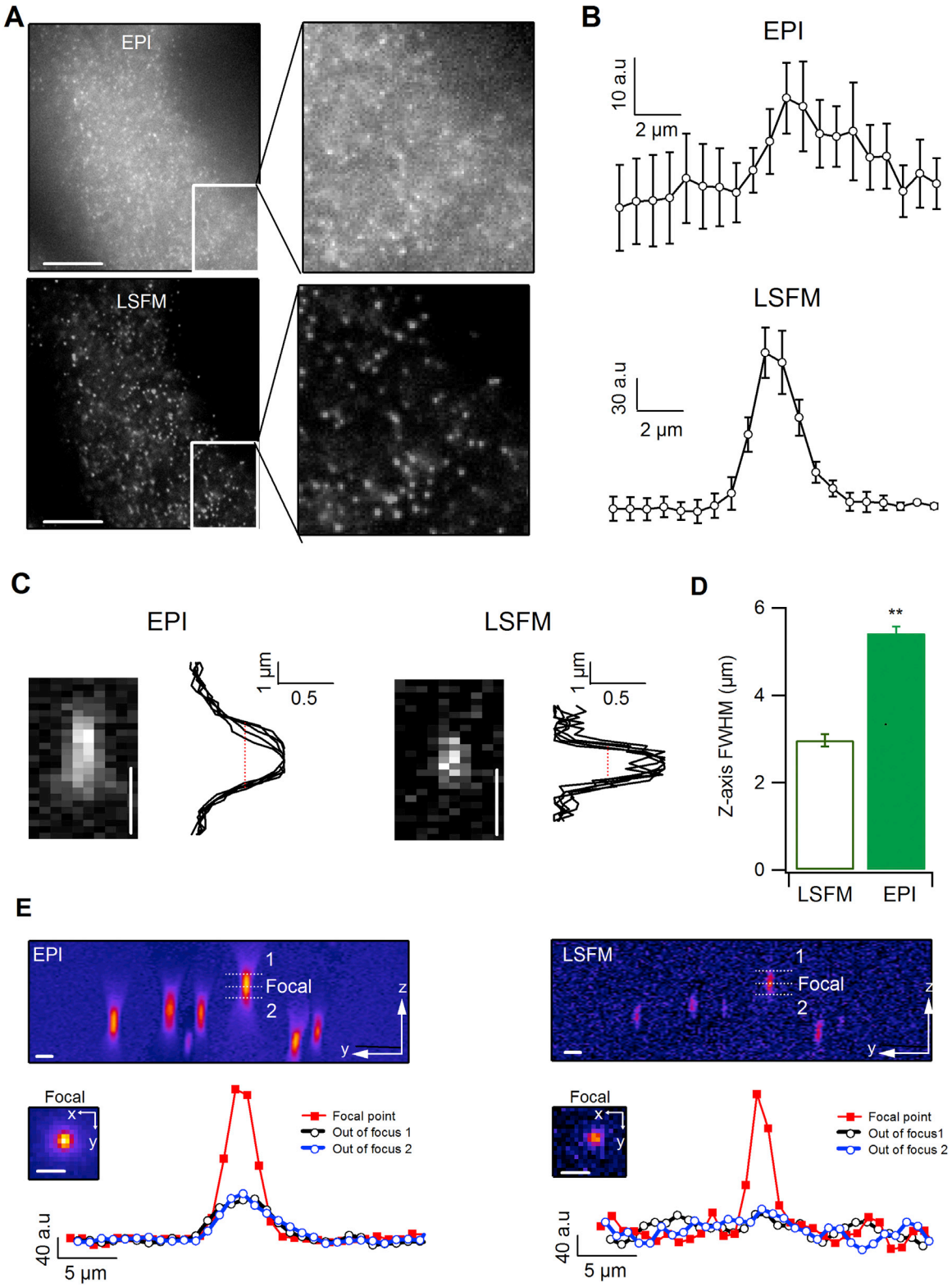

Fig. 3. Evaluation of LSFM performance with predefined sample. (A) Fluorescent beads of submicron size imaged by EPI illumination (*top*) and LSFM (*bottom*). **(B)** Average linescan profiles across the center of single beads (n = 10 per condition). **(C)** Representative axial fluorescence distribution (*z*-axis) of single beads. Linescan profiles of multiple trials are shown aside. **(D)** LSFM reduced the axial distortion compared to EPI images (n = 5 each). **(E)** Focal and out-of-focus fluorescence of micron-size beads (~4 μm), shown along the *z*-axis (*y*-*z* plane projection). Out-of-focus positions 1 and 2 were set at 10 μm above or below the focal plane. *Below*, representative linescan profiles along the lateral (*y*-axis) direction at different *z*-axis positions. The x-y section of the focal plane is shown in the zoomed images. Scale bars: 50 μm for *A*, and 10 μm for *E*.

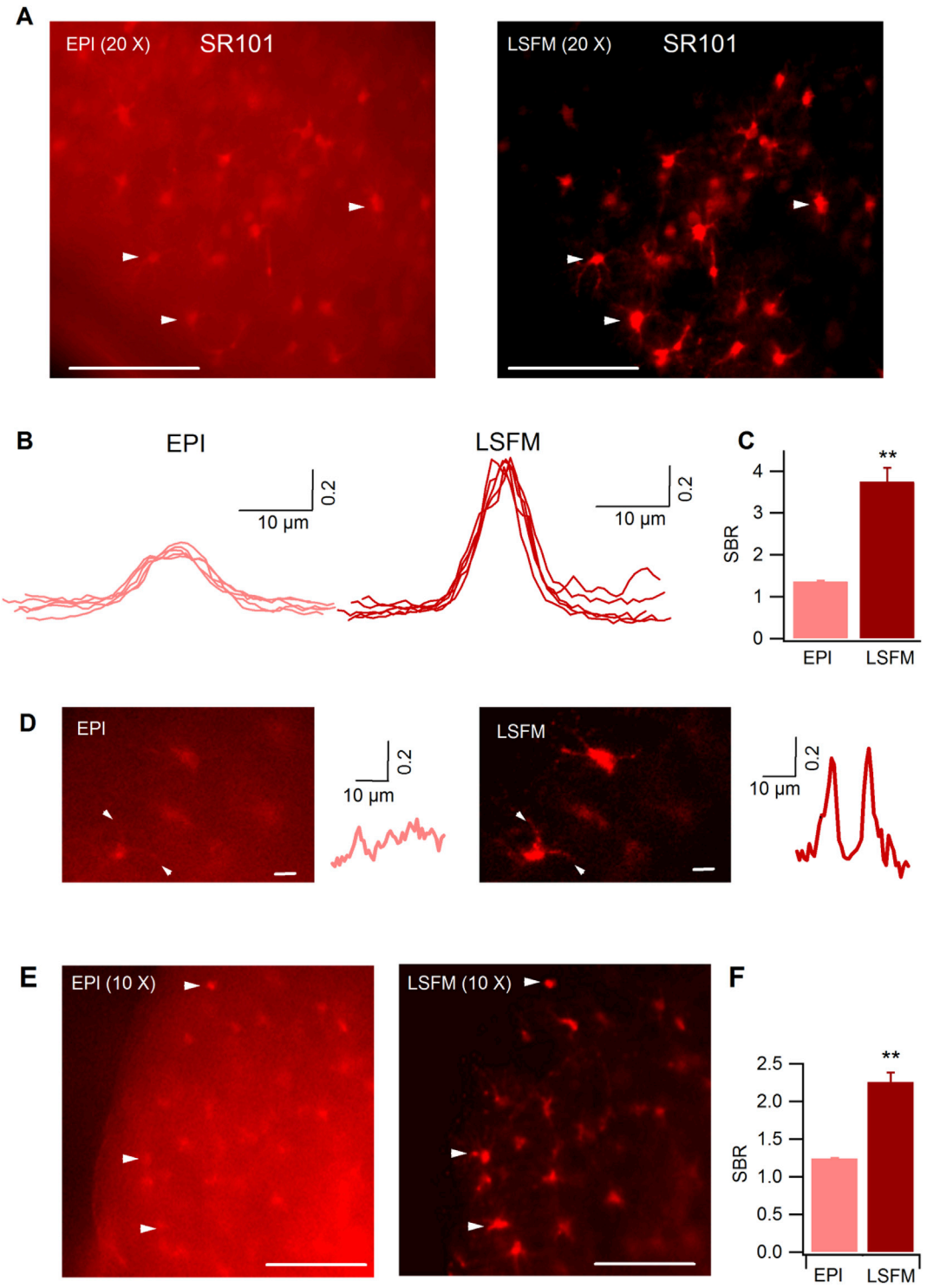

Fig. 4. Light sheet imaging of astrocytes in acute mouse brain slices. (A) SR101-stained astrocytes imaged by EPI and LSFM, respectively. A × 20 NA0.5 water immersion objective was used; arrow heads exemplify astrocytes visible in both conditions. **(B)** Linescan profiles of fluorescence distribution across the somata of single astrocytes (line position defined by the opposing arrowheads). **(C)** The signal to background ratio (SBR) quantified for single astrocytes ($p < 0.01$; $n = 20$ per condition). **(D)** Branches of SR101-stained astrocytes unveiled by LSFM, with linescan profiles shown aside. **(E-F)** Similar experiments carried out at lower-magnification (× 10 NA0.3; $n = 40$ per condition). Scale bars: 50 µm for *A*, 10 µm for *D*, and 100 µm for *E*.

SR101-positive astrocytes (Fig. S2C). In the absence of stimulus, the combination of LSFM and C-Screen revealed discrete active Ca^{2+} domains in astrocytes (Fig. 5A–B). LSFM-recorded Ca^{2+} signals displayed higher dynamic range and were twice as large on average relative to those detected by EPI imaging (Fig. 5C–D). The temporal correlations between Ca^{2+} signals of all active domains from light sheet imaging showed a broad distribution, suggesting a low-level of global synchronization ($r_{12} = 0.2 \pm 0.014$; Fig. 5E). Thanks to the wide-field configuration coupled with a digital camera, LSFM permitted astrocyte Ca^{2+} signals to be recorded at high acquisition rate (e.g., 20 Hz, Fig. 5F).

Complementary to chemical sensor, genetically encoded Ca^{2+} indicators enable calcium measurements in specific cell types (Akerboom

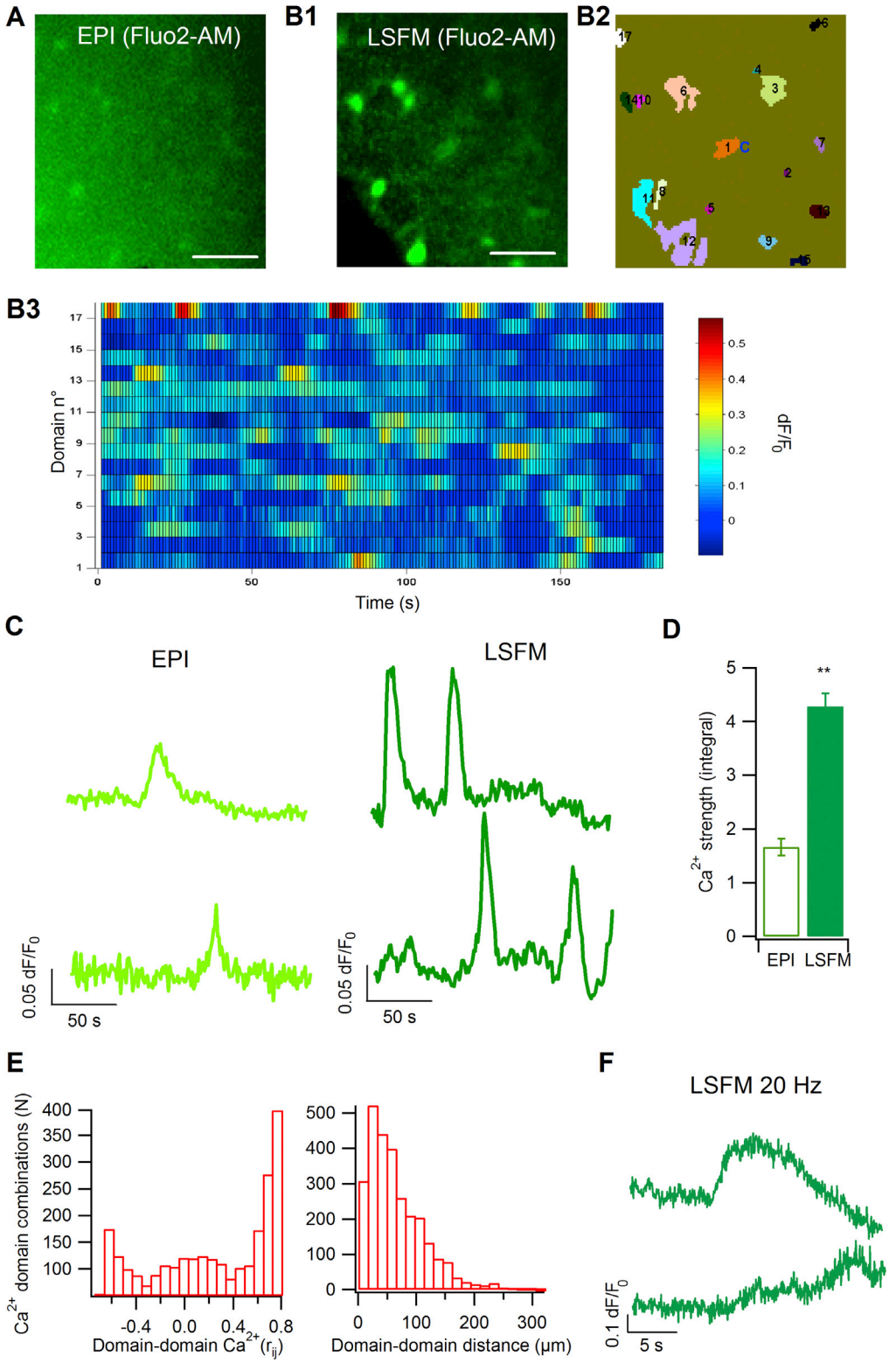

Fig. 5. Imaging astrocytic Ca^{2+} signals with chemical indicator. (A) Fluo2-labeled astrocytes viewed by EPI illumination in cortical slices. The same region was then imaged with LSFM **(B1)**. Ca^{2+}-active domains were detected by C-Screen analysis **(B2)**, with raster plot shown in **(B3)**. A × 10 NA0.3 water immersion objective was used. **(C)** Representative Ca^{2+} signals detected from EPI and LSFM time-lapse image stacks. **(D)** Comparison of Ca^{2+} signal strength quantified from temporal integral ($p < 0.01$; n = 188–299 responsive domains from 9 brain slices of 5 mice). **(E)** Distribution of temporal correlations between Ca^{2+} responses of all paired active domains (*left*), as an estimation of global synchronization. Right, histogram distribution of corresponding domain-domain distances (2775 paired domain combinations from 9 slices of 5 mice). **(F)** LSFM imaging of astrocytic Ca^{2+} signals at high acquisition rate (20 Hz). Representative movies from EPI and LSFM recordings are provided in the supplementary file. Scale bars: 50 µm.

et al., 2013) and are thought to influence less the intrinsic signals in targeted cells (Smith et al., 2018). We here used GCaMP6 that comprises circularly permuted GFP, the Ca^{2+}-sensitive protein calmodulin and the M13 fragment of the myosin light chain kinase (Baird et al., 1999; Nakai et al., 2001) (Chen et al., 2013). We expressed GCaMP6 selectively in astrocytes by crossing a Cre-dependent GCaMP6f mouse line (Madisen et al., 2015) with an inducible Glast-CreER^{T2} line where Cre recombinase is present in astrocytes (Slezak et al., 2007) (Fig. S3A). In bigenic GCaMP6/Glast-CreER^{T2} mice (Fig. S3B), tamoxifen induced apparent GCaMP6 expression in astrocyte-like cells (Fig. S3C). Dual-color fluorescent immunohistochemical statinging confirmed the colocalization of GCaMP6 with the astrocyte marker S100β (Fig. S3D).

Spontaneous Ca^{2+} dynamics in GCaMP6-expressing astrocytes were then imaged by LSFM. Compared to EPI illumination, light sheet excitation improved the dynamic range of Ca^{2+} signals and revealed more Ca^{2+}-active domains (Fig. 6A–C), echoing the observation with the chemical indicator. The global temporal correlation between Ca^{2+}-active domains was 0.16 ± 0.0073 (Fig. 6D), comparable to that derived from Fluo2 imaging (r_{12} = 0.2 ± 0.014), confirming that spontaneous Ca^{2+} signals are weakly correlated. Inhibition of neuronal activity with tetrodotoxin (TTX, 1 μM) failed to block the Ca^{2+} signals in astrocytes (Fig S4). For all combinations of Ca^{2+} domains, plotting domain-to-domain temporal Ca^{2+} correlations against their corresponding distances showed no dependence on distance (Fig. 6E). We also manually drew Ca^{2+} responsive domains by inspecting time-lapse images, which gave similar time courses as derived from C-Screen analysis (Fig S5). Finally, the wide-field optical sectioning of LSFM allowed to record GCaMP6 signal at high frame rates (e.g., 10 Hz, Fig. 6F), whereas the conventional two-photon setup reached only acquisition rate around 1 Hz using similar settings (pixel size 0.34 μm over a field of view ~170 × 170 μm) (Fig. S1D). High frequency LSFM imaging would help to observe Ca^{2+} events occurring at near-/sub-second levels, as exemplified in Fig. S6 (30 Hz) and reported previously (Di Castro et al., 2011; Gu et al., 2018; Panatier et al., 2011; Stobart et al., 2018). Together, these data show that LSFM enables high-sensitivity and high-speed imaging of astrocytic Ca^{2+} dynamics over a wide field of view.

3.4. Heterogeneous activity for cortical and hypothalamic astrocytes

Long considered as a homogeneous cellular population, astrocytes are being recognized to display heterogeneous properties across brain areas so as to coordinate the specific actions of local neural circuits (Chai et al., 2017; Covelo and Araque, 2018; Gourine et al., 2010). To gain insights into the functional heterogeneity of regionally defined astrocyte populations, we used LSFM to examine Ca^{2+} activities of astrocytes located in mouse somatosensory cortex and the paraventricular zone of hypothalamus, which are respectively engaged in the processing of sensory inputs and body metabolism signals (Clasadonte and Prevot, 2018; Giaume et al., 2009). Spontaneous Ca^{2+} signals were readily detected in GCaMP6-expressing astrocytes in acute brain slices (Fig. 7A), whereas signals in hypothalamic astrocytes showed more oscillatory changes than cortical astrocytes (Fig. 7B). Astrocytes respond to synaptically released neurontransmitters by GPCR signaling (Agulhon et al., 2008; Khakh and McCarthy, 2015). We then evoked astrocyte Ca^{2+} elevation by activating a Gq type GPCR, the α1 adrenergic receptor that is functionally expressed in astrocytes (Ding et al., 2013; Paukert et al., 2014). Application of α1 adrenergic receptor agonist phenylephrine (50 μM) to brain slices evoked distinct Ca^{2+} signals in cortical and hypothalamic astrocytes: the former responded with rises of few oscillations, whereas the latter showed more frequent transients during the evoked Ca^{2+} rise (Fig. 7C and E). Phenylephrine-evoked Ca^{2+} responses in astrocytes were inhibited by the α1 adrenergic receptor antagonist terazosin (Paukert et al., 2014) (Fig. S7), validating the involvement of this GPCR pathway. Ca^{2+} signals could be detected in both astrocytic somata and processes with LSFM (Fig. S8), as monitored by confocal and two-photon microscopy (Shigetomi et al., 2013; Srinivasan et al., 2015). While GCPR activation elevated astrocytic Ca^{2+} in both areas, hypothalamic astrocytes responded more strongly than cortical astrocytes (signal integral, 27.5 ± 2.3 vs. 21.5 ± 1.25 dF/F_0*s, $p < 0.01$; Fig. 7D). Furthermore, adrenergic GPCR activation increased the temporal correlation of Ca^{2+} signals for both cortical and hypothalamic astrocytes, indicating a higher degree of synchronization for evoked Ca^{2+} signals relative to spontaneous conditions (Fig. 7F). Together, these results show distinct Ca^{2+} kinetics between cortical and hypothalamic astrocytes.

4. Discussion

Here, we show that LSFM via wide-field optical sectioning allows for sensitive imaging of astrocyte Ca^{2+} signals in acute mouse brain slices. This approach revealed distinct Ca^{2+} signals between cortical and hypothalamic astrocytes, highlighting their activity heterogeneity. The light sheet configuration of two objectives separates the excitation and emission pathway, thereby facilitating the adjustment of the respective optical axes. For instance, imaging objectives of different magnifications and/or NA allow to select the field of view and the spatial resolution, while changing the excitation objective allows to tune the thickness and extent of the light sheet (Power and Huisken, 2017; Tian et al., 2019). Alternatively, LSFM can be also achieved by a single objective (Bouchard et al., 2015; Meddens et al., 2016), which facilitates imaging in conditions with limited spatial accessibility, but complicates the separate adjustment of the excitation and imaging pathway. Nevertheless, single-objective LSFM would facilitate in vivo recording to study astrocytes in a more native state (Zamanian et al., 2012). Since the light sheet plane can be digitally scanned (e.g., with a galvo mirror) along the *z*-axis (Bouchard et al., 2015; Power and Huisken, 2017; Tomer et al., 2015), LSFM will helpful for fast 3D imaging of astrocyte Ca^{2+} signals thus supporting on-going efforts to understand their physiological functions (Bindocci et al., 2017).

The continuous wave lasers used in the present study achieved penetration up to ~200 μm from the slice surface along the excitation direction. Nevertheless, the light sheet convergence within living mammalian tissues is inevitably affected by light scattering (Jacques, 2013). The use of pulsed infrared two-photon lasers and tunable acoustic gradient devices have increased tissue penetration of light sheet excitation (Wolf et al., 2015; Zong et al., 2015), at the expense of setup complexity and costs. LSFM can be coupled to different types of digital cameras to allow fast acquisition over a wide field of view (Keller and Dodt, 2012; Ritter et al., 2010). Moreover, the recent development of bright and ultrafast Ca^{2+} indicator (Dana et al., 2019) will help to reduce the exposure time for single images thus allow for higher acquisition rates. In this regard, light sheet imaging will help to follow over a wide field of view the fast Ca^{2+} events in astrocytes (Di Castro et al., 2011; Gu et al., 2018; Panatier et al., 2011; Stobart et al., 2018). On the other hand, the reliance on point-to-point scanning of conventional two-photon microscopy limits its use for fast image acquisition and may introduce artifacts in reconstituted images due to the desynchronized pixel sampling. Two-photon microscopes integrating newly designed scanning systems have improved the acquisition rate (Bindocci et al., 2017; Zong et al., 2017), though the additional components exacerbate the setup burden. Nevertheless, the digital scanning mode of two-photon microscope allows to zoom in regions of interest such as neuronal dendrites or single astrocytic processes for high speed acquisition, which is not provided by our LSFM approach. Considering the respective advantages of light sheet and two-photon excitation, the current study extends the method of choice for brain astrocyte activity imaging in specific experimental conditions.

Parallel to improving the quality of dynamic imaging, unbiased computational detection of Ca^{2+} domains in astrocyte networks is required. Maximal intensity projection of time-lapse images has been used as a rapid way to search astrocytic Ca^{2+} signals, where Ca^{2+} active domains in principle would imprint higher intensity in the projection image relative to inactive regions. Due to the uneven intracellular

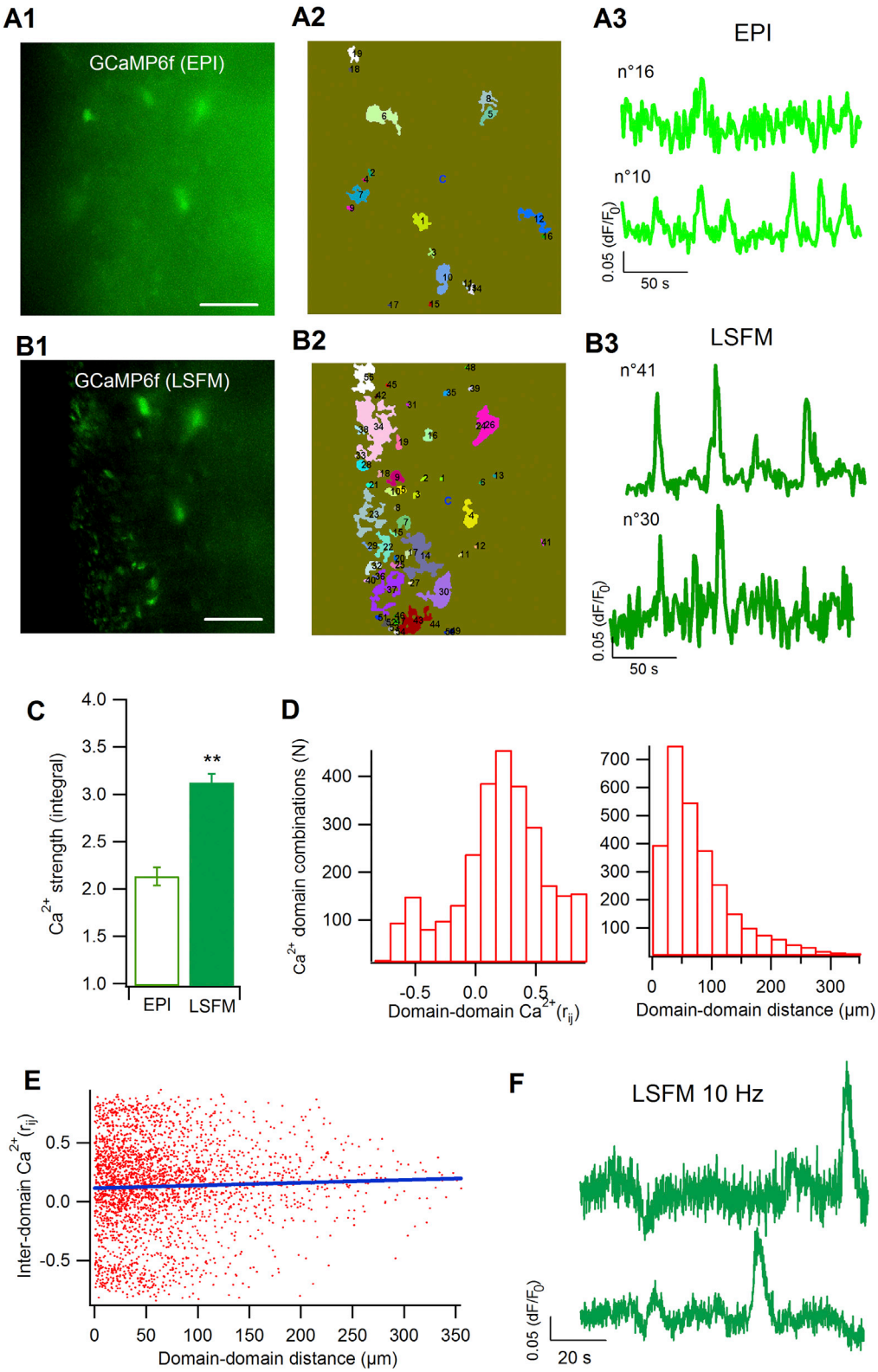

Fig. 6. Imaging astrocytic Ca^{2+} with genetically encoded sensor. Time-lapse imaging of GCaMP6-expressing astrocytes in acute cortical slices without (**A1-A3**, EPI) and with optical sectioning (**B1-B3,** LSFM). **(C)** Ca^{2+} signal strength compared for both conditions ($p < 0.01$; 220 - 359 active regions from 11 slices of 6–9 mice). **(D)** Histogram of temporal correlations for Ca^{2+} responses of paired domains (*left*), and their corresponding distances. Data were derived from 3156 pairs of Ca^{2+} domains from 11 slices of 9 mice. **(E)** Scatter plot depicting domain-domain Ca^{2+} correlations (i.e., synchronization level) against their distances. **(F)** Representative Ca^{2+} signals recorded at high frequency by LSFM (× 20 NA0.5 water immersion objective; 10 Hz). Representative movies for EPI and LSFM recordings are provided in the supplementary file. Scale bars: 50 µm.

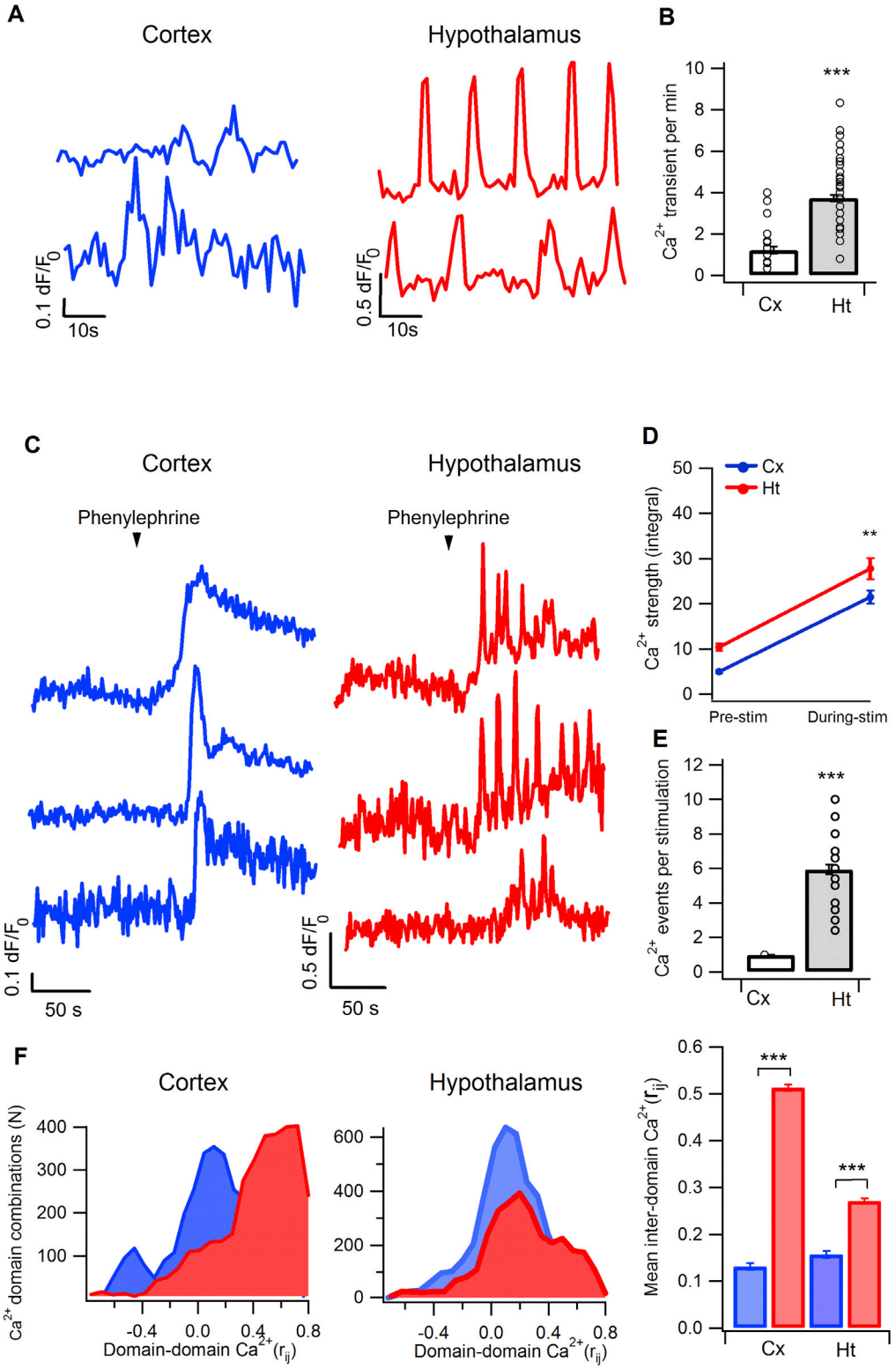

Fig. 7. Distinct features in Ca^{2+} signals in cortical and hypothalamic astrocytes. (A) Light-sheet imaging of spontaneous Ca^{2+} signals in astrocytes of mouse cortex and hypothalamus. GCaMP6 was expressed in astrocytes and the representative traces were from single Ca^{2+} domains. **(B)** Comparison of frequency of spontaneous Ca^{2+} oscillations for cortical (Cx) and hypothalamic (Ht) astrocytes (n = 57–67 cells from 15 slices of 11 mice per condition, $p < 0.001$). **(C)** Activation of adrenergic α1 receptors by phenylephrine (50 μM, bath perfusion for 60 s) evoked robust yet distinct Ca^{2+} elevations in astrocytes in cortex and hypothalamus. Representative traces were from different Ca^{2+} domains. **(D)** Signal strength of astrocytic Ca^{2+} signals pre- and during-stimulation as estimated by the temporal integral of normalized Ca^{2+} time courses (n = 314–345 active domains from 7-11 slices of 6 mice per condition). **(E)** Comparison of Ca^{2+} transients during phenylephrine stimulation (n = 44–72 cells from 11 slices of 8 mice, $p < 0.001$). **(F)** Phenylephrine stimulation enhanced the synchronization of astrocytic Ca^{2+} signals. Distributions of temporal correlations of Ca^{2+} signals from all active domains are shown in the histograms, blue denoting the data from spontaneous Ca^{2+} signals and red from phenylephrine-evoked signals (n = 3156–4415 pairs of Ca^{2+} domains from 7 - 15 slices of 6–9 mice per condition). Cx, cortex; Ht, hypothalamus; Pe, phenylephrine.

distribution of Ca^{2+} indicator, certain constantly bright areas showing no Ca^{2+} rises could also be registered that may mask the Ca^{2+}-active regions of lower intensity. We introduced here the principle of spatio-temporal correlation screening to detect locally correlated temporal signals. Clustered pixels showing synchronizing time courses were defined as responsive domains. Fluorescently visible structures that in fact showed no dynamic changes were excluded, while initially dim pixels that displayed later on fluorescence augmentation (i.e., Ca^{2+} rise) were picked up. Pearson's correlation coefficient relies mainly on the similarity of signal trends, while being relatively independent of the absolute intensity (Oheim and Li, 2007). Thus, screening of locally correlated signals helps to identify Ca^{2+} rises and improves their signal-to-noise ratio (Savtchouk et al., 2018; Wang et al., 2017). Ca^{2+} domains surrounding adjacent astrocytic structures may be merged together, which is due to the diffraction-limited fluorescence detection and the diffusion of Ca^{2+} bursts to nearby domains. A further step will be to incorporate temporal segmentation to isolate functional domains displaying activities at different time points. The computational time for C-Screen is in the order of tens of seconds and thus slower than the very rapid maximal intensity projection. Since imaging condition and quantification requirements vary in different contexts, a combination or an evaluation per se of different computational methods will help to improve the detection of astrocytic Ca^{2+} signals (Agarwal et al., 2017; Srinivasan et al., 2015) (Wang et al., 2019).

Astrocytes display Ca^{2+} activities spontaneously and in response to GPCR activation, as observed in brain slices (Di Castro et al., 2011; Shigetomi et al., 2018) and in vivo (Agarwal et al., 2017; Bindocci et al., 2017; Hirase et al., 2004; Paukert et al., 2014). Light sheet imaging unveiled distinct features in Ca^{2+} activities between cortical and hypothalamic astrocytes, thus reinforcing the evidence for heterogeneous astrocyte subpopulations that show different molecular, morphological and functional properties (Ben Haim and Rowitch, 2017; Chai et al., 2017; Lanjakornsiripan et al., 2018; Martin-Fernandez et al., 2017). Astrocyte heterogeneity appears necessary to coordinate the action of local neural circuits that are adapted to specific physiological inputs and outputs. Considering that astrocyte spontaneous Ca^{2+} activity is modulated by Ca^{2+}-permeable channels (Shigetomi et al., 2011) and the internal stores (Wang et al., 2006), the different spontaneous Ca^{2+} kinetics observed between cortical and hypothalamic astrocytes likely reflect the distinct recruitment of Ca^{2+} handling pathways. Accordingly, we observed that astrocytes of both regions differ also in their response to α1 adrenergic receptor activation in terms of kinetics and signal strength. Astrocyte Ca^{2+} kinetics is shaped by the intercellular communication of astrocyte populations (Gu et al., 2018), as well as the Ca^{2+} level in internal stores and their Ca^{2+} buffering capacity (Bazargani and Attwell, 2015; Li et al., 2012). Moreover, the distinct organization of local neuronal circuits may shape the astrocytic Ca^{2+} responses (Chai et al., 2017). To fully resolve the mechanisms underlying the heterogeneities in astrocyte Ca^{2+} signals will require further investigations. In view of the on-going challenge on understanding the function of astrocyte Ca^{2+} signaling in neurophysiology (Bazargani and Attwell, 2015; Fiacco and McCarthy, 2018; Savtchouk and Volterra, 2018), quantitative light sheet imaging represents a complementary strategy for mechanistic investigations. Moreover, beyond Ca^{2+} signals, this methodology will also helps to measure other dynamics signals by adopting pathway-specific fluorescent sensors.

Declaration of competing interest

The authors declare no competing interests.

CRediT authorship contribution statement

Cuong Pham: Methodology, Investigation, Formal analysis, Writing - original draft, Visualization, Writing - review & editing. **Daniela Herrera Moro:** Methodology, Validation, Resources, Writing - review & editing. **Christine Mouffle:** Resources. **Steve Didienne:** Resources. **Régine Hepp:** Methodology, Resources, Writing - review & editing. **Frank W. Pfrieger:** Resources, Writing - review & editing. **Jean-Marie Mangin:** Methodology, Resources. **Pascal Legendre:** Formal analysis, Resources, Writing - review & editing. **Claire Martin:** Resources, Writing - review & editing. **Serge Luquet:** Project administration, Resources, Writing - review & editing. **Bruno Cauli:** Project administration, Resources, Writing - review & editing. **Dongdong Li:** Conceptualization, Methodology, Investigation, Writing - original draft, Writing - review & editing, Supervision.

Acknowledgments

We thank the animal facility and imaging platform of the IBPS (Sorbonne Université, Paris, France). We also thank Gael Launay and Cyprian Wozniak for helping to set up the light sheet microscope, Anne-Cecile Boulay for ALDH1L1-EGFP mice and Ludovic Tricoire for help on two-photon setup, and Martin Oheim and Nicole Ropert for early discussions on the data analysis procedures. This work was supported by the Agence Nationale de la Recherche (ANR-15-CE14-0030; ANR-17-CE37-0010-03), National Natural Science Foundation of China (N° 31628005; N° 31929003), and Fondation pour la Recherche Médicale.

Appendix A. Supplementary data

Supplementary data to this article can be found online at https://doi.org/10.1016/j.neuroimage.2020.117069.

References

Agarwal, A., Wu, P.H., Hughes, E.G., Fukaya, M., Tischfield, M.A., Langseth, A.J., Wirtz, D., Bergles, D.E., 2017. Transient opening of the mitochondrial permeability transition pore induces microdomain calcium transients in astrocyte processes. Neuron 93, 587–605 e587.

Agulhon, C., Petravicz, J., McMullen, A.B., Sweger, E.J., Minton, S.K., Taves, S.R., Casper, K.B., Fiacco, T.A., McCarthy, K.D., 2008. What is the role of astrocyte calcium in neurophysiology? Neuron 59, 932–946.

Ahrens, M.B., Orger, M.B., Robson, D.N., Li, J.M., Keller, P.J., 2013. Whole-brain functional imaging at cellular resolution using light-sheet microscopy. Nat. Methods 10, 413–420.

Akerboom, J., Carreras Calderon, N., Tian, L., Wabnig, S., Prigge, M., Tolo, J., Gordus, A., Orger, M.B., Severi, K.E., Macklin, J.J., Patel, R., Pulver, S.R., Wardill, T.J., Fischer, E., Schuler, C., Chen, T.W., Sarkisyan, K.S., Marvin, J.S., Bargmann, C.I., Kim, D.S., Kugler, S., Lagnado, L., Hegemann, P., Gottschalk, A., Schreiter, E.R., Looger, L.L., 2013. Genetically encoded calcium indicators for multi-color neural activity imaging and combination with optogenetics. Front. Mol. Neurosci. 6, 2.

Appaix, F., Girod, S., Boisseau, S., Romer, J., Vial, J.C., Albrieux, M., Maurin, M., Depaulis, A., Guillemain, I., van der Sanden, B., 2012. Specific in vivo staining of astrocytes in the whole brain after intravenous injection of sulforhodamine dyes. PloS One 7, e35169.

Baird, G.S., Zacharias, D.A., Tsien, R.Y., 1999. Circular permutation and receptor insertion within green fluorescent proteins. Proc. Natl. Acad. Sci. U. S. A. 96, 11241–11246.

Bazargani, N., Attwell, D., 2015. Astrocyte calcium signaling: the third wave. Nat. Neurosci. 19, 182–189.

Ben Haim, L., Rowitch, D.H., 2017. Functional diversity of astrocytes in neural circuit regulation. Nat. Rev. Neurosci. 18, 31–41.

Bindocci, E., Savtchouk, I., Liaudet, N., Becker, D., Carriero, G., Volterra, A., 2017. Three-dimensional Ca(2+) imaging advances understanding of astrocyte biology. Science 356.

Bonnot, A., Guiot, E., Hepp, R., Cavellini, L., Tricoire, L., Lambolez, B., 2014. Single-fluorophore biosensors based on conformation-sensitive GFP variants. Faseb. J. 28, 1375–1385.

Bouchard, M.B., Voleti, V., Mendes, C.S., Lacefield, C., Grueber, W.B., Mann, R.S., Bruno, R.M., Hillman, E.M., 2015. Swept confocally-aligned planar excitation (SCAPE) microscopy for high speed volumetric imaging of behaving organisms. Nat. Photon. 9, 113–119.

Cahoy, J.D., Emery, B., Kaushal, A., Foo, L.C., Zamanian, J.L., Christopherson, K.S., Xing, Y., Lubischer, J.L., Krieg, P.A., Krupenko, S.A., Thompson, W.J., Barres, B.A., 2008. A transcriptome database for astrocytes, neurons, and oligodendrocytes: a new resource for understanding brain development and function. J. Neurosci. 28, 264–278.

Cauli, B., Hamel, E., 2018. Brain perfusion and astrocytes. Trends Neurosci. 41, 409–413.

Chai, H., Diaz-Castro, B., Shigetomi, E., Monte, E., Octeau, J.C., Yu, X., Cohn, W., Rajendran, P.S., Vondriska, T.M., Whitelegge, J.P., Coppola, G., Khakh, B.S., 2017. Neural circuit-specialized astrocytes: transcriptomic, proteomic, morphological, and functional evidence. Neuron 95, 531–549 e539.

Chen, T.W., Wardill, T.J., Sun, Y., Pulver, S.R., Renninger, S.L., Baohan, A., Schreiter, E.R., Kerr, R.A., Orger, M.B., Jayaraman, V., Looger, L.L., Svoboda, K., Kim, D.S., 2013. Ultrasensitive fluorescent proteins for imaging neuronal activity. Nature 499, 295–300.
Clasadonte, J., Prevot, V., 2018. The special relationship: glia-neuron interactions in the neuroendocrine hypothalamus. Nat. Rev. Endocrinol. 14, 25–44.
Covelo, A., Araque, A., 2018. Neuronal activity determines distinct gliotransmitter release from a single astrocyte. Elife 7, e32237.
Dallerac, G., Zapata, J., Rouach, N., 2018. Versatile control of synaptic circuits by astrocytes: where, when and how? Nat. Rev. Neurosci. 19, 729–743.
Dana, H., Sun, Y., Mohar, B., Hulse, B.K., Kerlin, A.M., Hasseman, J.P., Tsegaye, G., Tsang, A., Wong, A., Patel, R., Macklin, J.J., Chen, Y., Konnerth, A., Jayaraman, V., Looger, L.L., Schreiter, E.R., Svoboda, K., Kim, D.S., 2019. High-performance calcium sensors for imaging activity in neuronal populations and microcompartments. Nat. Methods 16, 649–657.
Deo, C., Lavis, L.D., 2018. Synthetic and genetically encoded fluorescent neural activity indicators. Curr. Opin. Neurobiol. 50, 101–108.
Di Castro, M.A., Chuquet, J., Liaudet, N., Bhaukaurally, K., Santello, M., Bouvier, D., Tiret, P., Volterra, A., 2011. Local Ca2+ detection and modulation of synaptic release by astrocytes. Nat. Neurosci. 14, 1276–1284.
Ding, F., O'Donnell, J., Thrane, A.S., Zeppenfeld, D., Kang, H., Xie, L., Wang, F., Nedergaard, M., 2013. alpha1-Adrenergic receptors mediate coordinated Ca2+ signaling of cortical astrocytes in awake, behaving mice. Cell Calcium 54, 387–394.
Fiacco, T.A., Agulhon, C., Taves, S.R., Petravicz, J., Casper, K.B., Dong, X., Chen, J., McCarthy, K.D., 2007. Selective stimulation of astrocyte calcium in situ does not affect neuronal excitatory synaptic activity. Neuron 54, 611–626.
Fiacco, T.A., McCarthy, K.D., 2018. Multiple lines of evidence indicate that gliotransmission does not occur under physiological conditions. J. Neurosci. 38, 3–13.
Giaume, C., Koulakoff, A., Roux, L., Holcman, D., Rouach, N., 2010. Astroglial networks: a step further in neuroglial and gliovascular interactions. Nat. Rev. Neurosci. 11, 87–99.
Giaume, C., Maravall, M., Welker, E., Bonvento, G., 2009. The barrel cortex as a model to study dynamic neuroglial interaction. Neuroscientist 15, 351–366.
Gourine, A.V., Kasymov, V., Marina, N., Tang, F., Figueiredo, M.F., Lane, S., Teschemacher, A.G., Spyer, K.M., Deisseroth, K., Kasparov, S., 2010. Astrocytes control breathing through pH-dependent release of ATP. Science 329, 571–575.
Gu, X., Chen, W., Volkow, N.D., Koretsky, A.P., Du, C., Pan, Y., 2018. Synchronized astrocytic Ca^{2+} responses in neurovascular coupling during somatosensory stimulation and for the resting state. Cell Rep. 23, 3878–3890.
Hirase, H., Qian, L., Bartho, P., Buzsaki, G., 2004. Calcium dynamics of cortical astrocytic networks in vivo. PLoS Biol. 2, E96.
Jacques, S.L., 2013. Optical properties of biological tissues: a review. Phys. Med. Biol. 58, R37–R61.
Jemielita, M., Taormina, M.J., Delaurier, A., Kimmel, C.B., Parthasarathy, R., 2013. Comparing phototoxicity during the development of a zebrafish craniofacial bone using confocal and light sheet fluorescence microscopy techniques. J. Biophot. 6, 920–928.
Jiang, R., Diaz-Castro, B., Looger, L.L., Khakh, B.S., 2016. Dysfunctional calcium and glutamate signaling in striatal astrocytes from huntington's disease model mice. J. Neurosci. 36, 3453–3470.
Keller, P.J., Ahrens, M.B., 2015. Visualizing whole-brain activity and development at the single-cell level using light-sheet microscopy. Neuron 85, 462–483.
Keller, P.J., Dodt, H.U., 2012. Light sheet microscopy of living or cleared specimens. Curr. Opin. Neurobiol. 22, 138–143.
Khakh, B.S., McCarthy, K.D., 2015. Astrocyte calcium signaling: from observations to functions and the challenges therein. Cold Spring Harbor Perspect. Biol. 7, a020404.
Kuga, N., Sasaki, T., Takahara, Y., Matsuki, N., Ikegaya, Y., 2011. Large-scale calcium waves traveling through astrocytic networks in vivo. J. Neurosci. 31, 2607–2614.
Lanjakornsiripan, D., Pior, B.J., Kawaguchi, D., Furutachi, S., Tahara, T., Katsuyama, Y., Suzuki, Y., Fukazawa, Y., Gotoh, Y., 2018. Layer-specific morphological and molecular differences in neocortical astrocytes and their dependence on neuronal layers. Nat. Commun. 9, 1623.
Li, D., Herault, K., Isacoff, E.Y., Oheim, M., Ropert, N., 2012. Optogenetic activation of LiGluR-expressing astrocytes evokes anion channel-mediated glutamate release. J. Physiol. 590, 855–873.
Li, D., Xiong, J., Qu, A., Xu, T., 2004. Three-Dimensional tracking of single secretory granules in live PC12 cells. Biophys. J. 87, 1991–2001.
Lin, M.Z., Schnitzer, M.J., 2016. Genetically encoded indicators of neuronal activity. Nat. Neurosci. 19, 1142–1153.
Lobas, M.A., Tao, R., Nagai, J., Kronschlager, M.T., Borden, P.M., Marvin, J.S., Looger, L.L., Khakh, B.S., 2019. A genetically encoded single-wavelength sensor for imaging cytosolic and cell surface ATP. Nat. Commun. 10, 711.
Lock, J.T., Parker, I., Smith, I.F., 2015. A comparison of fluorescent Ca(2)(+) indicators for imaging local Ca(2)(+) signals in cultured cells. Cell Calcium 58, 638–648.
Madisen, L., Garner, A.R., Shimaoka, D., Chuong, A.S., Klapoetke, N.C., Li, L., van der Bourg, A., Niino, Y., Egolf, L., Monetti, C., Gu, H., Mills, M., Cheng, A., Tasic, B., Nguyen, T.N., Sunkin, S.M., Benucci, A., Nagy, A., Miyawaki, A., Helmchen, F., Empson, R.M., Knopfel, T., Boyden, E.S., Reid, R.C., Carandini, M., Zeng, H., 2015. Transgenic mice for intersectional targeting of neural sensors and effectors with high specificity and performance. Neuron 85, 942–958.
Martin-Fernandez, M., Jamison, S., Robin, L.M., Zhao, Z., Martin, E.D., Aguilar, J., Benneyworth, M.A., Marsicano, G., Araque, A., 2017. Synapse-specific astrocyte gating of amygdala-related behavior. Nat. Neurosci. 20, 1540–1548.
Meddens, M.B., Liu, S., Finnegan, P.S., Edwards, T.L., James, C.D., Lidke, K.A., 2016. Single objective light-sheet microscopy for high-speed whole-cell 3D super-resolution. Biomed. Optic Express 7, 2219–2236.
Mutze, J., Iyer, V., Macklin, J.J., Colonell, J., Karsh, B., Petrasek, Z., Schwille, P., Looger, L.L., Lavis, L.D., Harris, T.D., 2012. Excitation spectra and brightness optimization of two-photon excited probes. Biophys. J. 102, 934–944.
Nakai, J., Ohkura, M., Imoto, K., 2001. A high signal-to-noise Ca2+ probe composed of a single green fluorescent protein. Nat. Biotechnol. 19, 137–141.
Nedergaard, M., Verkhratsky, A., 2012. Artifact versus reality-How astrocytes contribute to synaptic events? Glia 60, 1013–1023.
Nimmerjahn, A., Kirchhoff, F., Kerr, J.N., Helmchen, F., 2004. Sulforhodamine 101 as a specific marker of astroglia in the neocortex in vivo. Nat. Methods 1, 31–37.
Oheim, M., Li, D., 2007. Quantitative colocalisation imaging: concepts, measurements, and pitfalls. In: Shorte, S.L., Frischknecht, F. (Eds.), Imaging Cellular and Molecular Biological Functions. Springer, pp. 117–156.
Otsu, Y., Couchman, K., Lyons, D.G., Collot, M., Agarwal, A., Mallet, J.M., Pfrieger, F.W., Bergles, D.E., Charpak, S., 2015. Calcium dynamics in astrocyte processes during neurovascular coupling. Nat. Neurosci. 18, 210–218.
Panatier, A., Vallee, J., Haber, M., Murai, K.K., Lacaille, J.C., Robitaille, R., 2011. Astrocytes are endogenous regulators of Basal transmission at central synapses. Cell 146, 785–798.
Paukert, M., Agarwal, A., Cha, J., Doze, V.A., Kang, J.U., Bergles, D.E., 2014. Norepinephrine controls astroglial responsiveness to local circuit activity. Neuron 82, 1263–1270.
Perez-Alvarez, A., Araque, A., Martin, E.D., 2013. Confocal microscopy for astrocyte in vivo imaging: recycle and reuse in microscopy. Front. Cell. Neurosci. 7, 51.
Perez-Alvarez, A., Navarrete, M., Covelo, A., Martin, E.D., Araque, A., 2014. Structural and functional plasticity of astrocyte processes and dendritic spine interactions. J. Neurosci. 34, 12738–12744.
Pologruto, T.A., Sabatini, B.L., Svoboda, K., 2003. ScanImage: flexible software for operating laser scanning microscopes. Biomed. Eng. Online 2, 13.
Power, R.M., Huisken, J., 2017. A guide to light-sheet fluorescence microscopy for multiscale imaging. Nat. Methods 14, 360–373.
Reeves, A.M., Shigetomi, E., Khakh, B.S., 2011. Bulk loading of calcium indicator dyes to study astrocyte physiology: key limitations and improvements using morphological maps. J. Neurosci. 31, 9353–9358.
Ritter, J.G., Veith, R., Veenendaal, A., Siebrasse, J.P., Kubitscheck, U., 2010. Light sheet microscopy for single molecule tracking in living tissue. PloS One 5, e11639.
Robin, L.M., Oliveira da Cruz, J.F., Langlais, V.C., Martin-Fernandez, M., Metna-Laurent, M., Busquets-Garcia, A., Bellocchio, L., Soria-Gomez, E., Papouin, T., Varilh, M., Sherwood, M.W., Belluomo, I., Balcells, G., Matias, I., Bosier, B., Drago, F., Van Eeckhaut, A., Smolders, I., Georges, F., Araque, A., Panatier, A., Oliet, S.H.R., Marsicano, G., 2018. Astroglial CB1 receptors determine synaptic D-serine availability to enable recognition memory. Neuron 98, 935–944.
Santello, M., Toni, N., Volterra, A., 2019. Astrocyte function from information processing to cognition and cognitive impairment. Nat. Neurosci. 22, 154–166.
Savtchouk, I., Carriero, G., Volterra, A., 2018. Studying axon-astrocyte functional interactions by 3D two-photon Ca(2+) imaging: a practical guide to experiments and "big data" analysis. Front. Cell. Neurosci. 12, 98.
Savtchouk, I., Volterra, A., 2018. Gliotransmission: beyond black-and-white. J. Neurosci. 38, 14–25.
Schmidt, E.M., Oheim, M., 2018. Two-photon Imaging Induces Brain Heating and Calcium Microdomain Hyper-Activity in Cortical Astrocytes bioRxiv 321091.
Shigetomi, E., Bushong, E.A., Haustein, M.D., Tong, X., Jackson-Weaver, O., Kracun, S., Xu, J., Sofroniew, M.V., Ellisman, M.H., Khakh, B.S., 2013. Imaging calcium microdomains within entire astrocyte territories and endfeet with GCaMPs expressed using adeno-associated viruses. J. Gen. Physiol. 141, 633–647.
Shigetomi, E., Hirayama, Y.J., Ikenaka, K., Tanaka, K.F., Koizumi, S., 2018. Role of purinergic receptor P2Y1 in spatiotemporal Ca(2+) dynamics in astrocytes. J. Neurosci. 38, 1383–1395.
Shigetomi, E., Kracun, S., Sofroniew, M.V., Khakh, B.S., 2010. A genetically targeted optical sensor to monitor calcium signals in astrocyte processes. Nat. Neurosci. 13, 759–766.
Shigetomi, E., Tong, X., Kwan, K.Y., Corey, D.P., Khakh, B.S., 2011. TRPA1 channels regulate astrocyte resting calcium and inhibitory synapse efficacy through GAT-3. Nat. Neurosci. 15, 70–80.
Slezak, M., Goritz, C., Niemiec, A., Frisen, J., Chambon, P., Metzger, D., Pfrieger, F.W., 2007. Transgenic mice for conditional gene manipulation in astroglial cells. Glia 55, 1565–1576.
Smith, N.A., Kress, B.T., Lu, Y., Chandler-Militello, D., Benraiss, A., Nedergaard, M., 2018. Fluorescent Ca(2+) indicators directly inhibit the Na,K-ATPase and disrupt cellular functions. Sci. Signal. 11, eaal2039.
Srinivasan, R., Huang, B.S., Venugopal, S., Johnston, A.D., Chai, H., Zeng, H., Golshani, P., Khakh, B.S., 2015. Ca^{2+} signaling in astrocytes from Ip3r2(-/-) mice in brain slices and during startle responses in vivo. Nat. Neurosci. 18, 708–717.
Stobart, J.L., Ferrari, K.D., Barrett, M.J.P., Gluck, C., Stobart, M.J., Zuend, M., Weber, B., 2018. Cortical circuit activity evokes rapid astrocyte calcium signals on a similar timescale to neurons. Neuron 98, 726–735 e724.
Svoboda, K., Yasuda, R., 2006. Principles of two-photon excitation microscopy and its applications to neuroscience. Neuron 50, 823–839.
Swedlow, J.R., 2013. Quantitative fluorescence microscopy and image deconvolution. Methods Cell Biol. 114, 407–426.
Tian, Q., Hu, J., Xie, C., Mei, K., Pham, C., Mo, X., Hepp, R., Soares, S., Nothias, F., Wang, Y., Liu, Q., Cai, F., Zhong, B., Li, D., Yao, J., 2019. Recovery from tachyphylaxis of TRPV1 coincides with recycling to the surface membrane. Proc. Natl. Acad. Sci. U. S. A. 116, 5170–5175.

Tomer, R., Lovett-Barron, M., Kauvar, I., Andalman, A., Burns, V.M., Sankaran, S., Grosenick, L., Broxton, M., Yang, S., Deisseroth, K., 2015. SPED light sheet microscopy: fast mapping of biological system structure and function. Cell 163, 1796–1806.

Wang, T.F., Zhou, C., Tang, A.H., Wang, S.Q., Chai, Z., 2006. Cellular mechanism for spontaneous calcium oscillations in astrocytes. Acta Pharmacol. Sin. 27, 861–868.

Wang, Y., DelRosso, N.V., Vaidyanathan, T.V., Cahill, M.K., Reitman, M.E., Pittolo, S., Yu, G., Poskanzer, K.E., 2019. Accurate quantification of astrocyte and neurotransmitter fluorescence dynamics for single-cell and population-level physiology. Nat. Neurosci. 22, 1936–1944.

Wang, Y., Shi, G., Miller, D.J., Wang, C., Broussard, G., Tian, L., Yu, G., 2017. Automated functional analysis of astrocytes from chronic time-lapse calcium imaging data. Front. Neuroinf. 11, 48.

Wolf, S., Supatto, W., Debregeas, G., Mahou, P., Kruglik, S.G., Sintes, J.M., Beaurepaire, E., Candelier, R., 2015. Whole-brain functional imaging with two-photon light-sheet microscopy. Nat. Methods 12, 379–380.

Zamanian, J.L., Xu, L., Foo, L.C., Nouri, N., Zhou, L., Giffard, R.G., Barres, B.A., 2012. Genomic analysis of reactive astrogliosis. J. Neurosci. 32, 6391–6410.

Zhao, Y., Zhang, Y., Liu, X., Lv, X., Zhou, W., Luo, Q., Zeng, S., 2009. Photostimulation of astrocytes with femtosecond laser pulses. Optic Express 17, 1291–1298.

Zong, W., Wu, R., Li, M., Hu, Y., Li, Y., Li, J., Rong, H., Wu, H., Xu, Y., Lu, Y., Jia, H., Fan, M., Zhou, Z., Zhang, Y., Wang, A., Chen, L., Cheng, H., 2017. Fast high-resolution miniature two-photon microscopy for brain imaging in freely behaving mice. Nat. Methods 14, 713–719.

Zong, W., Zhao, J., Chen, X., Lin, Y., Ren, H., Zhang, Y., Fan, M., Zhou, Z., Cheng, H., Sun, Y., Chen, L., 2015. Large-field high-resolution two-photon digital scanned light-sheet microscopy. Cell Res. 25, 254–257.